IOPscience iopscience.iop.org

Home Search Collections Journals About Contact us My IOPscience

Temperature-dependent yield effects on composite beams used in CMOS MEMS

This content has been downloaded from IOPscience. Please scroll down to see the full text.

2013 J. Micromech. Microeng. 23 035023

(http://iopscience.iop.org/0960-1317/23/3/035023)

View the table of contents for this issue, or go to the journal homepage for more

Download details:

IP Address: 140.113.38.11
This content was downloaded on 26/04/2014 at 07:16

Please note that terms and conditions apply.

J. Micromech. Microeng. **23** (2013) 035023 (8pp) doi:10.1088/0960-1317/23/3/035023

Temperature-dependent yield effects on composite beams used in CMOS MEMS

F Y Kuo[1,2], C S Chang[1,3], Y S Liu[1,2], K A Wen[1,2] and L S Fan[1,2,4]

[1] Rm. 316, Microelectronics and Information Systems Research Center, No.1001, Daxue Rd., East Dist., Hsinchu City 300, Taiwan, Republic of China
[2] Institute of Electronics, National Chiao Tung University, Hsinchu, Taiwan, Republic of China
[3] Global Sensing Core, Inc., Hsinchu, Taiwan, Republic of China
[4] Institute of Nano Engineering and MicroSystems, National Tsing Hua University, Hsinchu, Taiwan, Republic of China

E-mail: fykuo.tw@gmail.com, chaosen0414@gmail.com (C S Chang), thomas.ee99g@nctu.edu.tw (Y S Liu), stellawen@mail.nctu.edu.tw and lsfan@ieee.org

Received 6 August 2012, in final form 16 January 2013
Published 1 February 2013
Online at stacks.iop.org/JMM/23/035023

Abstract
This paper presents an experimentally verified analytical model of temperature-dependent yield effects on the curvatures of composite beam structures used in complementary metal–oxide semiconductor microelectromechanical systems (CMOS MEMS). The temperature-dependent effects on composite beam curvatures of a thermal process can be predicted by extracting key parameters from the measured curvatures of a limited number of CMOS MEMS composite-layer combinations. The effects due to thermal history in MEMS packaging, which change the characteristics of beam curvatures due to material yield, are further analyzed. The models are verified with measured results from beam structures fabricated by an application-specific integrated circuit-compatible 0.18 μm 1P6M CMOS MEMS process using a white light interferometer. These models can be applied in electronic design automation tools to provide good prediction of temperature-dependent properties related to CMOS MEMS beam curvature, such as sensing capacitance, for monolithic sensor system on chip design.

(Some figures may appear in colour only in the online journal)

1. Introduction

Sensor integration has attracted significant attention in recent years for enabling the sensing and processing of multiple environmental intelligences on a single electronics device. One integration approach is to integrate the complementary metal–oxide semiconductor (CMOS) circuit and microelectromechanical systems (MEMS) sensors on a compact monolithic substrate [1, 2]. Monolithic integration of these MEMS structures with circuits by the CMOS MEMS process may reduce overall chip size and avoid non-reproducible parasitic components and additional signal losses due to interconnection between the sensor and the circuit. Post-CMOS MEMS processing is commonly adopted and made compatible with the conventional CMOS application-specific integrated circuit (ASIC) process [3–5]. For these CMOS MEMS processes, however, MEMS structures made up of the composite layers of metal and oxide experience temperature-dependent deformation due to residual stresses and variation of thermal stresses. The cantilever beam element, for example, is widely used in MEMS sensors and actuators including sensing fingers of the MEMS accelerometer [6], radio frequency (RF) MEMS switch [7], etc. The variation of the curvature of beams in these MEMS sensor designs may cause variation of sensing capacitance, which brings uncertainty to sensor read-out circuit design specifications and overall microsystem performances. The complicate residual stress distribution within composite layers at a given operation temperature makes it difficult to predict beam curvatures accurately in CMOS MEMS processes. To describe the composite-layer behavior, several analytical formulas have been discussed [16] for accurate modeling of elastic deformation of MEMS structures due to residual stress, from simple structures [14, 15] to multilayer structures, including the extension of

 © 2013 IOP Publishing Ltd Printed in the UK & the USA

the Stoney formula [18] and analysis based on the continuity of strain among layers [19]. These works can be used to develop test patterns to extract residual stresses of fabricated multilayer MEMS structures [17]. However, temperature dependence for deformation modeling was not considered in these works. On the other hand, generalized formulas [8] and matrix forms [9] for curvature radius and layer stresses modeling caused by thermal strain in semiconductor multilayer structures have been developed. The analysis of temperature dependence of a three-metal CMOS process by introducing the coefficient of thermal expansion (CTE) is studied [10]. Extended modeling and validation for large-displacement beam actuator applications based on the matrix forms have also been proposed [11]. In this paper, we analyze and provide the temperature-dependent analytical model of the beam curvature of all the different layer combinations allowed by a complete ASIC-compatible CMOS process. The numerical values of beam curvatures can be predicted by key parameter extraction from the experimental data. The model covers the packaging thermal effects of the MEMS capping process on the beam curvatures due to material yield. This model can be used in computer-aided design tools to provide good prediction of temperature-dependent properties related to CMOS MEMS beam curvature, such as sensing capacitance, needed for the sensor system on chip (SOC) design. We also validate the analytical model with measurement results for all the different oxide–metal-layer combinations using a 1P6M 0.18 μm ASIC-compatible CMOS MEMS process.

2. ASIC-compatible 1P6M CMOS MEMS process

A complete ASIC-compatible 1P6M CMOS MEMS process includes the foundry standard 1P6M CMOS process and the MEMS post-CMOS micromachining process. The microstructures are constructed by a dry-etch-based post-process. First, a hard mask (HM) layer is deposited on the standard CMOS wafer to define the MEMS structure. Second, a thick photoresist is coated to protect the non-MEMS area. Third, the microstructures are defined by anisotropic reactive ion etch of dielectrics. Fourth, an isotropic silicon undercut process is adopted to release the microstructures. Figure 1 shows the sectional view of CMOS MEMS process flow step by step. The movable structures are made from the stack of interconnect layers in conventional CMOS technology. Different metal layers can be electrically connected by using via in IMD. Additional metal layer is utilized as an HM layer to define high aspect ratio microstructures from damage. The post-process achieves high aspect ratio structures with excellent flexibility of wiring.

The standard CMOS process allows combinations of the presence of six-metal layers, M1–M6. To observe the characteristics of the beam curvature of the process, cantilever finger structures with 25–32 different combinations of M1–M5 metal layers are observed at 9 different zones on test keys. Top metal layer M6 is preserved to improve the reliability of measurement using a Zygo white light interferometer.

The packaging process is necessary for the MEMS device to protect microstructures. Wafer level capping by glass frit is

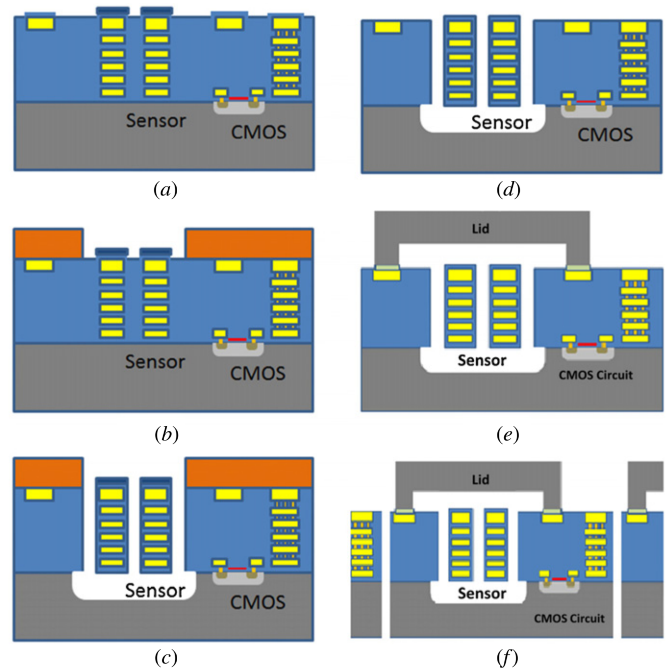

Figure 1. Sectional view of the CMOS-MEMS structure.

adopted in this process. The silicon cap wafer is pre-etched to reserve the space of the MEMS device, and then glass frit is printed on the bond ring by screen printing. After the soft cure process, the cap wafer is placed on the CMOS wafer with precise alignment, and then wafer to wafer bonding gets completed during stress and the hot cure process. The temperature of hot cure is about 350 °C. The capping process is shown in figures 1(*e*) and (*f*). It is worth noting that glass capping is adopted in the experiment to allow the white light interferometer to measure the beam curvature through the transparent glass caps.

3. Analytical model for beam curvature

Consider a multilayer cantilever structure with N layers. Each layer i has a set of process/material properties $X_i = \{t_i, \alpha_i, \sigma_i, E_i\}$ where t_i is the layer thickness, α_i is the temperature expansion coefficient, σ_i is the residual stress under reference temperature T_o and E_i is the effective Young's modulus. For a given metal–oxide combinations, the layer properties of all N layers can be denoted as $X = \{X_1, \ldots, X_N\}$.

3.1. Calculation of radius of curvature

We derived the out-of-plane curl due to stress gradient in the cantilever as follows. The stress gradient produces the deformation with the radius of curvature ρ. The force along the z-axis (perpendicular to the curling beam layer) can be expressed as

$$f(z) = (\sigma(z) + \Delta\varepsilon E(z))\, w\, \mathrm{d}z, \tag{1}$$

where $\Delta\varepsilon$ is the internal strain of the curling beam generated to cancel the force of gradient residual stress. $\sigma(z)$ and $E(z)$ are defined piecewise as

$$E(z) = \begin{cases} E_1, & z \leqslant t_1 \\ E_2, & t_1 < z \leqslant t_1 + t_2 \\ \vdots & \\ E_i, & \sum_{i-1} t_k < z \leqslant \sum_{i} t_k \end{cases}$$
$$\sigma(z) = \begin{cases} \sigma_1 + \alpha_1 E(z)\Delta T, & z \leqslant t_1 \\ \sigma_2 + \alpha_2 E(z)\Delta T, & t_1 < z \leqslant t_1 + t_2 \\ \vdots & \\ \sigma_i + \alpha_n E(z)\Delta T, & \sum_{i-1} t_k < z \leqslant \sum_{i} t_k \end{cases}, \tag{2}$$

where $\Delta T = T - T_o$ under the temperature T.

The net force for the beam shall be zero. Therefore, $\Delta\varepsilon$ can be derived from the following equation:

$$\int_o^{\Sigma t} (\sigma(z) + \Delta\varepsilon E(z))\,\mathrm{d}z = 0$$
$$\Rightarrow \Delta\varepsilon = -\int_o^{\Sigma t} \sigma(z)\,\mathrm{d}z \Big/ \int_o^{\Sigma t} E(z)\,\mathrm{d}z = -S/E, \tag{3}$$

where

$$S = \int_o^{\Sigma t} \sigma(z)\,\mathrm{d}z, \quad E = \int_o^{\Sigma t} E(z)\,\mathrm{d}z.$$

The neutral axis $z = z_o$ of a composite-layer beam shall meet the following condition:

$$\int_o^{\Sigma t} E(z)(z - z_o)\,\mathrm{d}z = 0$$
$$\Rightarrow z_o = \int_o^{\Sigma t} E(z)z\,\mathrm{d}z \Big/ \int_o^{\Sigma t} E(z)\,\mathrm{d}z = E_z/E, \tag{4}$$

where

$$E_z = \int_o^{\Sigma t} E(z)z\,\mathrm{d}z.$$

Considering the curling beam due to the residual stress, the radius of curvature ρ shall meet the zero-moment criteria:

$$\int_o^{\Sigma t} \sigma_b(z - z_o)\,\mathrm{d}z = 0,$$

where

$$\sigma_b = \left[(\sigma(z) + \Delta\varepsilon E(z)) - \frac{E(z)}{\rho}(z - z_o)\right]. \tag{5}$$

Here, σ_b is the internal stress distribution as a function of z.

Based on (3) and (4), we may rewrite (5) and derive the beam curvature $1/\rho$:

$$S_z - \frac{E_z}{E}S - \frac{E_{z^2}}{\rho} = 0$$
$$\Rightarrow \frac{1}{\rho} = \frac{1}{E_{z^2}}\left(S_z - \frac{E_z}{E}S\right), \tag{6}$$

where

$$S_z = \int_o^{\Sigma t} \sigma(z)z\,\mathrm{d}z, \quad E_{z^2} = \int_o^{\Sigma t} E(z)(z - z_o)^2\,\mathrm{d}z.$$

Table 1. Oxide and metal layer parameters for the simplified model.

	X_o		X_m
t_o	0.8 μm	t_m	0.58 μm
σ_o (extracted)	100 MPa	σ_m (extracted)	−110 Mpa
Ey_1	65 GPa	Ey_2	69 Gpa
α_o	8.5e−6/°C	α_m	2.3e−5/°C

3.2. Simplified model and parameter extraction

For convenience, we define a binary coding rule to represent a given layer combination i as $\mathbf{R}M_1M_2M_3M_4M_5M_6$, where M_x is 1 if layer x metal exists, and zero otherwise. For example, R000001 represents the structure where M1–M5 layers do not exist and only the M6 layer exists. It is the second combination, so it is numbered as 2 in 64-layer combinations. For a simplified model of a multi-layer structure with the same oxide layer property $X_o = \{t_o, \alpha_o, \sigma_o, Ey_1\}$ and the same metal layer property $X_m = \{t_m, \alpha_m, \sigma_m, Ey_2\}$, the curvature $1/\rho$ of the second combination R000001 under the six-metal CMOS MEMS process can be calculated as

$$\begin{aligned}
&-(t_m(210\,Ey2\,\sigma_o - 210Ey1\,\sigma_m)t_o^2 \\
&\quad + t_m^2(390\,Ey2\,\sigma_o - 390\,Ey1\,\sigma_m)t_o \\
&\quad + t_m^3(180\,Ey2\,\sigma_o - 180\,Ey1\,\sigma_m))/ \\
&\quad \big(2401Ey1^2t_o^4 + (868\,Ey1\,Ey2 + 7364\,Ey1^2)t_m t_o^3 \\
&\quad + (2382\,Ey1\,Ey2 + 8202\,Ey1^2)t_m^2\,t_o^2 \\
&\quad + (2188\,Ey1\,Ey2 + 3860\,Ey1^2)t_m^3\,t_o \\
&\quad + (Ey2^2 + 670\,Ey1\,Ey2 + 625\,Ey1^2)t_m^4\big).
\end{aligned}$$

Another example of the 63rd combination R111110 (all metals exist except M6) is

$$\begin{aligned}
&(t_m(210\,Ey2\,\sigma_o - 210Ey1\,\sigma_m)t_o^2 \\
&\quad + t_m^2(390\,Ey2\,\sigma_o - 390\,Ey1\,\sigma_m)t_o \\
&\quad + t_m^3(180\,Ey2\,\sigma_o - 180\,Ey1\,\sigma_m))/ \\
&\quad \big(2401Ey1^2t_o^4 + (2660\,Ey1\,Ey2 + 5572\,Ey1^2)t_m t_o^3 \\
&\quad + (600\;Ey2^2 + 5910\,Ey1\,Ey2 + 4074\,Ey1^2)t_m^2\,t_o^2 \\
&\quad + (1200\,Ey2^2 + 3980\,Ey1\,Ey2 + 868\,Ey1^2)t_m^3\,t_o \\
&\quad + (625\,Ey2^2 + 670\,Ey1\,Ey2 + Ey1^2)t_m^4\big).
\end{aligned}$$

Given the layer thickness and typical Young's modulus of metal and oxide layers for the CMOS MEMS process, we may extract residual stress of σ_m and σ_o by least-squares error minimization with beam curvature measurements of all or part of layer combinations with an offset. The residual stresses determine the slope and shape of the curvature versus layer combination curve and are independent of the curve offset in the simplified model. Therefore, residual stresses and offset can be extracted separately. Figure 2 shows the best curve fit of 32 measurements for the simplified model with parameters in table 1.

Even numbers of layer combinations (32 combinations) are compared in figure 2, since M6 is always present in our measurements as mentioned previously. The presence of each metal layer may have positive or negative contribution to the beam curvature, and the layer combination is binary coded. Therefore, the curve in figure 2 appears zig-zag and periodic

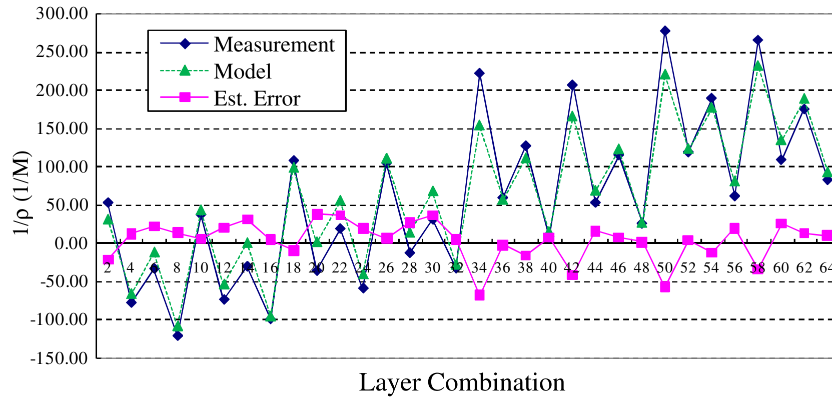

Figure 2. Estimation error of the simplified model with measurement results.

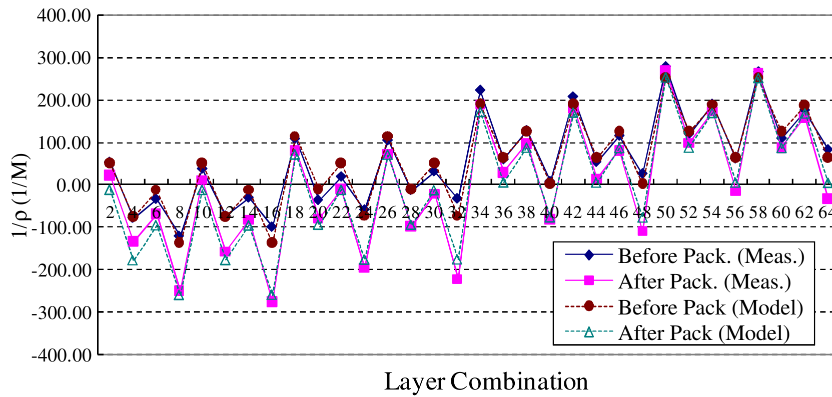

Figure 3. Estimation error of measurement data before and after packaging process.

in some sense. The average estimation error to curvature ratio is defined as the root square of the squared estimation error sum to squared curvature sum ratio. It is around 24% in this case with the offset value 185. From the analytical model, the other factor that determines the contribution of each layer to beam curvature is layer thickness. Therefore, the error of the simplified model can be further reduced by applying more accurate layer thickness of each layer in the CMOS MEMS process.

The complete analytical model can be imported into the electronic design automation (EDA) simulation tool using the Verilog-A format, and further incorporate with the curvature-to-capacitance model to derive a temperature-dependent sensing capacitance model of the cantilever beam with different oxide/metal combination for a given CMOS MEMS process. To model the temperature dependence of beam curvature at temperature T, the residual stress of any layer σ can be substituted by $\sigma = \sigma_o + \alpha\, E\, \Delta T$, where σ_o is the residual stress at the reference temperature T_o.

3.3. Material yield due to high temperature packaging process

Figure 3 shows the parameter extraction result for measurement data before and after the high temperature packaging process for capping. Beam curvatures change significantly after the process. Based on the proposed model,

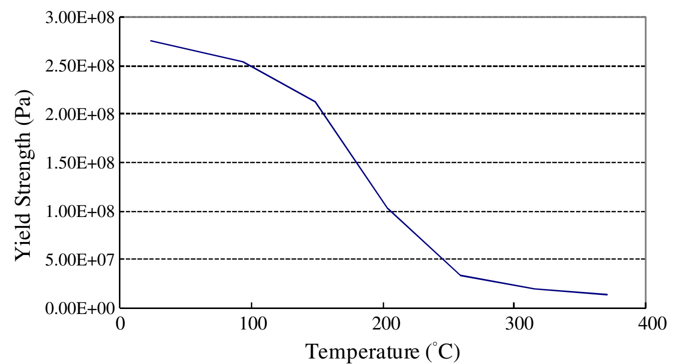

Figure 4. Yield strength versus temperature for aluminum.

the parameters before and after the packaging process are extracted. From the analytical model, it is found that the term $(\sigma_o\, Ey_2 – \sigma_m Ey_1)$ in numerator dominates the trend of the curvature. The extracted parameters show that $(\sigma_o\, Ey_2 – \sigma_m Ey_1)$ is about 2.03×10^{19} before packaging and $(\sigma_o\, Ey_2 – \sigma_m Ey_1)$ is increased to 2.66×10^{19} after the thermal process. The change of the term is further analyzed.

The highest temperature for the CMOS MEMS packaging process is around 350 °C. During heating, the thermal expansion of composite materials introduces significant internal stress. At the same time, the yield strength drops at high temperature, as shown in figure 4 [12]. When the

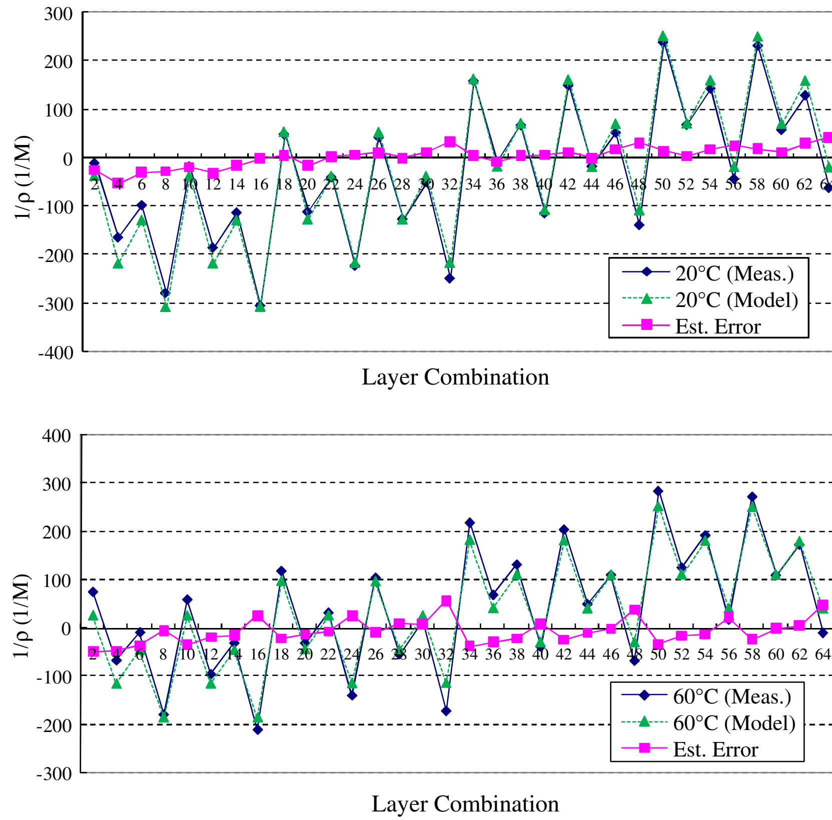

Figure 5. Estimated curvature and estimation error for 20 and 60 °C with the proposed model.

Table 2. Extracted residual stress and curvature estimation error after capping.

	20 °C	40 °C	60 °C
Est. σ_o @ T_o (MPa)	130	130	130
Est. σ_m @ T_o (MPa)	{M1∼M5} : {−230, −240, −270, −300, −305}		
	M6: −285	M6: −245	M6: −195
Est. MSE ratio of curvature (offset = 250)	13.8%	14.4%	14.5%

stress reaches the yield strength of the material, especially metal layers, the material begins to deform plastically and releases the residual stress of metal layers. When the structure anneals and returns to normal temperature, the structure may accumulate more stress due to contraction. In section 3.4, the thermal history of the packaging process will be analyzed in more detail.

3.4. Projection on curvature change due to thermal expansion

Figure 5 shows the modeling error after parameter extraction for beam curvature after the high temperature packaging (capping) process, at 20, 40 and 60 °C with typical CTE α_m and α_o applied to the residual stress $\sigma = \sigma_o + \alpha\ E\ \Delta T$. Table 2 shows the estimated residual stresses and mean square error of estimated curvature values to actual measurements (MSE) with parameter extraction for 20, 40 and 60 °C. It is found that the residual stress distribution of metal layers M1–M5 is not uniform as the simplified model in section 3.2 assumes. Table 2 shows that residual stresses of M1–M5 are different but invariant with the temperature, while M6 changes with the temperature. In the following section, the distribution of residual stress due to metal yield is discussed.

3.5. Estimation of yield point based on stress distribution

Based on the derived temperature dependency model, we observe the stress distribution of cross section for each layer of the composite beam structure. Figure 6(*a*) shows an example for stress distribution after the high temperature packaging process. The maximum stress –374 MPa appears near the bottom of the M1 layer for R100001. We further look into the temperature dependency of the maximum stress for each combination, and find that the maximum stress of all combinations is zero crossing at 190.2 °C. Figure 6(*b*) shows examples of R000101 and R100001. Considering that the yield stress of the aluminum drops rapidly around 200 °C, the result suggests that the common zero crossing temperature may indicate the point that most metal layers yield.

To further analyze the yield state of metal layers, we revisit the internal stress σ_b of metal layers in (5). When the metal starts to yield at high temperature, σ_b is constraint by the tensile yield strength Y of the metal

$$\sigma_b = \min\left[Y,\ (\sigma(z) + \Delta\varepsilon E(z)) - \frac{E(z)}{\rho}(z - z_o)\right]. \qquad (7)$$

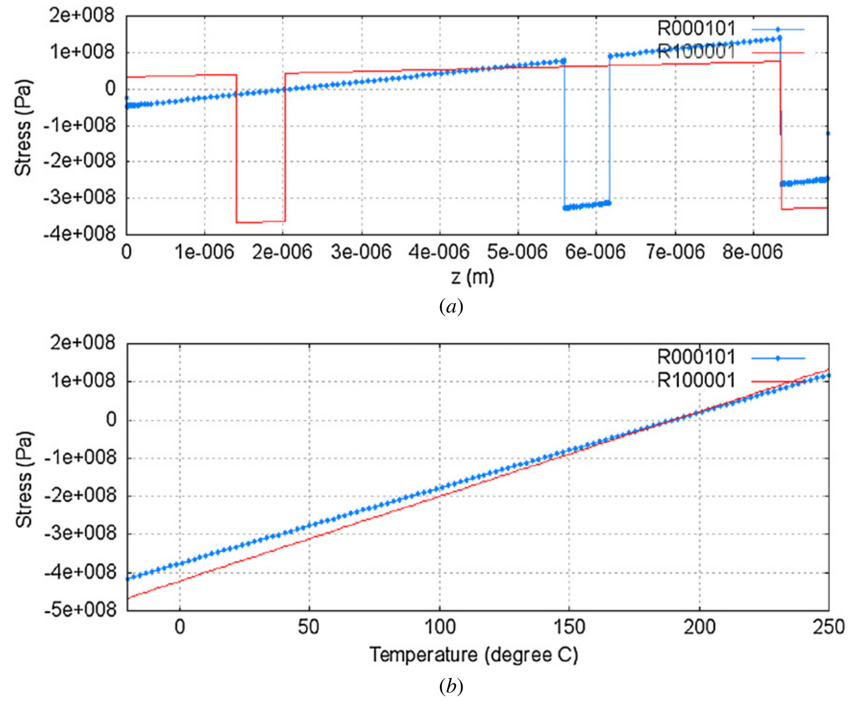

Figure 6. Stress distribution along z-axis cross section (where 0 of the x-axis represents the bottom side where M1 is located) and temperature T (°C) dependency of maximum stress for the combinations R000101 and R100001.

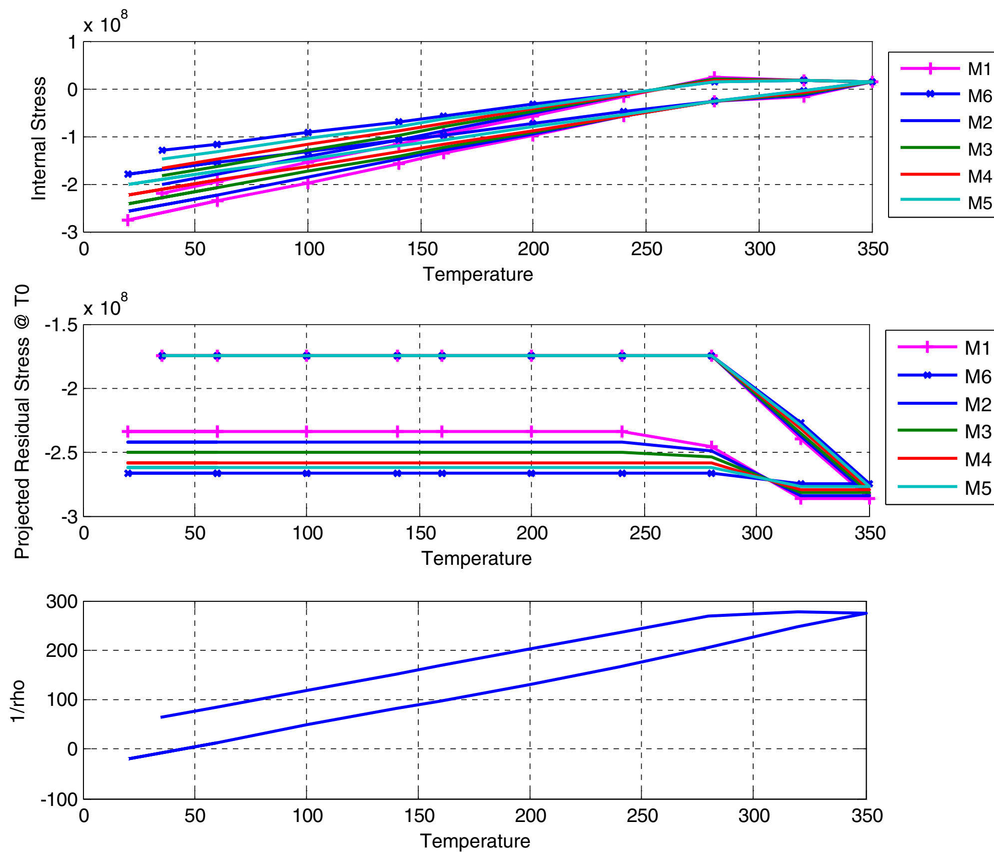

Figure 7. Internal stress and projected residual stress σ_m of each metal layer at T_o with tensile and compressive yields (R111111).

Table 3. Estimated residual stress and curvature with CTE scaling.

	20 °C	40 °C	60 °C
Est. σ_o (MPa)	201	225	253
Est. Error ratio of curvature by yield analysis ($K = 1.4$)	14%	15%	23%
Est. Error ratio of curvature by residual stress extraction in section 3.4	13.8%	14.4%	14.5%

Table 4. CAS tool output example for the simplified model in section 3.2.

R000001
$-(t_m(210\,Ey2\,\sigma_o - 210Ey1\,\sigma_m)t_o^2 + t_m^2(390\,Ey2\,\sigma_o - 390\,Ey2\,\sigma_m)t_o + t_m^3(180\,Ey2\,\sigma_o - 180\,Ey1\,\sigma_m))$
$(2188\,Ey1\,Ey2 + 3860\,Ey1^2)t_m^3\,t_o + (Ey2^2 + 670\,Ey1\,Ey2 + 625\,Ey1^2)t_m^4)$
$(t_m(210\,Ey2\,\sigma_o - 210Ey1\,\sigma_m)t_o^2 + t_m^2(390\,Ey2\,\sigma_o - 390\,Ey1\,\sigma_m)t_o + t_m^3(180\,Ey2\,\sigma_o - 180\,Ey1\,\sigma_m))/$
$(2401\,Ey1^2\,t_o^4 + (868\,Ey1\,Ey2 + 7364\,Ey1^2)\,t_m\,t_o^3 + (2382\,Ey1\,Ey2 + 8202\,Ey1^2)t_m^2\,t_o^2$
$+(2188\,Ey1\,Ey2 + 3860\,Ey1^2)t_m^3\,t_o + (Ey2^2 + 670\,Ey1\,Ey2 + 625\,Ey1^2)t_m^4)$
R000011
$-(t_m(336\,Ey2\,\sigma_o - 336Ey1\,\sigma_m)t_o^2 + t_m^2(624\,Ey2\,\sigma_o - 624\,Ey1\,\sigma_m)t_o + t_m^3(288\,Ey2\,\sigma_o - 288\,Ey1\,\sigma_m))$
$(24\,Ey2^2 + 3416\,Ey1\,Ey2 + 2608\,Ey1^2)t_m^3\,t_o + (16\,Ey2^2 + 1024\,Ey1\,Ey2 + 256\,Ey1^2)t_m^4)$
$(t_m(336\,Ey2\,\sigma_o - 336Ey1\,\sigma_m)t_o^2 + t_m^2(624\,Ey2\,\sigma_o - 624\,Ey1\,\sigma_m)t_o + t_m^3(288\,Ey2\,\sigma_o - 288\,Ey1\,\sigma_m))/$
$(2401\,Ey1^2\,t_o^4 + (1400\,Ey1\,Ey2^2 + 6832\,Ey1^2)\,t_m\,t_o^3 + (12\,Ey2^2 + 3780\,Ey1\,Ey2 + 6792\,Ey1^2)t_m^2\,t_o^2$
$+(24\,Ey2^2 + 3416\,Ey1\,Ey2 + 2608\,Ey1^2)t_m^3\,t_o + (16\,Ey2^2 + 1024\,Ey1\,Ey2 + 256\,Ey1^2)t_m^4)$
R000101
$-(t_m(252\,Ey2\,\sigma_o - 252Ey1\,\sigma_m)t_o^2 + t_m^2(468\,Ey2\,\sigma_o - 468\,Ey1\,\sigma_m)t_o + t_m^3(216\,Ey2\,\sigma_o - 216\,Ey1\,\sigma_m))$
$(96\,Ey2^2 + 2816\,Ey1\,Ey2 + 3136\,Ey1^2)t_m^3\,t_o + (52\,Ey2^2 + 808\,Ey1\,Ey2 + 436\,Ey1^2)t_m^4)$
$(t_m(252\,Ey2\,\sigma_o - 252Ey1\,\sigma_m)t_o^2 + t_m^2(468\,Ey2\,\sigma_o - 468\,Ey1\,\sigma_m)t_o + t_m^3(216\,Ey2\,\sigma_o - 216\,Ey1\,\sigma_m))/$
$(2401\,Ey1^2\,t_o^4 + (1232\,Ey1\,Ey2 + 7000\,Ey1^2)\,t_m\,t_o^3 + (48\,Ey2^2 + 3228\,Ey1\,Ey2 + 7308\,Ey1^2)t_m^2\,t_o^2$
$+(96\,Ey2^2 + 2816\,Ey1\,Ey2 + 3136\,Ey1^2)t_m^3\,t_o + (52\,Ey2^2 + 808\,Ey1\,Ey2 + 436\,Ey1^2)t_m^4)$
R000111
$-(t_m(378\,Ey2\,\sigma_o - 378Ey1\,\sigma_m)t_o^2 + t_m^2(702\,Ey2\,\sigma_o - 702\,Ey1\,\sigma_m)t_o + t_m^3(324\,Ey2\,\sigma_o - 324\,Ey1\,\sigma_m))$
$(144\,Ey2^2 + 3996\,Ey1\,Ey2 + 1908\,Ey1^2)t_m^3\,t_o + (81\,Ey2^2 + 1134\,Ey1\,Ey2 + 81\,Ey1^2)t_m^4)$
$(t_m(378\,Ey2\,\sigma_o - 378Ey1\,\sigma_m)t_o^2 + t_m^2(702\,Ey2\,\sigma_o - 702\,Ey1\,\sigma_m)t_o + t_m^3(324\,Ey2\,\sigma_o - 324\,Ey1\,\sigma_m))/$
$(2401\,Ey1^2\,t_o^4 + (1764\,Ey1\,Ey2 + 6468\,Ey1^2)\,t_m\,t_o^3 + (72\,Ey2^2 + 4602\,Ey1\,Ey2 + 5910\,Ey1^2)t_m^2\,t_o^2$
$+(144\,Ey2^2 + 3996\,Ey1\,Ey2 + 1908\,Ey1^2)t_m^3\,t_o + (81\,Ey2^2 + 1134\,Ey1\,Ey2 + 81\,Ey1^2)t_m^4)$
R001001
$-(t_m(168\,Ey2\,\sigma_o - 168\,Ey1\,\sigma_m)t_o^2 + t_m^2(312\,Ey2\,\sigma_o - 312\,Ey1\,\sigma_m)t_o + t_m^3(144\,Ey2\,\sigma_o - 144\,Ey1\,\sigma_m))$
$(216\,Ey2^2 + 2576\,Ey1\,Ey2 + 3256\,Ey1^2)t_m^3\,t_o + (112\,Ey2^2 + 688\,Ey1\,Ey2 + 496\,Ey1^2)t_m^4)$
$(t_m(168\,Ey2\,\sigma_o - 168\,Ey1\,\sigma_m)t_o^2 + t_m^2(312\,Ey2\,\sigma_o - 312\,Ey1\,\sigma_m)t_o + t_m^3(144\,Ey2\,\sigma_o - 144\,Ey1\,\sigma_m))/$
$(2401\,Ey1^2\,t_o^4 + (1232\,Ey1\,Ey2 + 7000\,Ey1^2)\,t_m\,t_o^3 + (108\,Ey2^2 + 3108\,Ey1\,Ey2 + 7368\,Ey1^2)t_m^2\,t_o^2$
$+(216\,Ey2^2 + 2576\,Ey1\,Ey2 + 3256\,Ey1^2)t_m^3\,t_o + (112\,Ey2^2 + 688\,Ey1\,Ey2 + 496\,Ey1^2)t_m^4)$

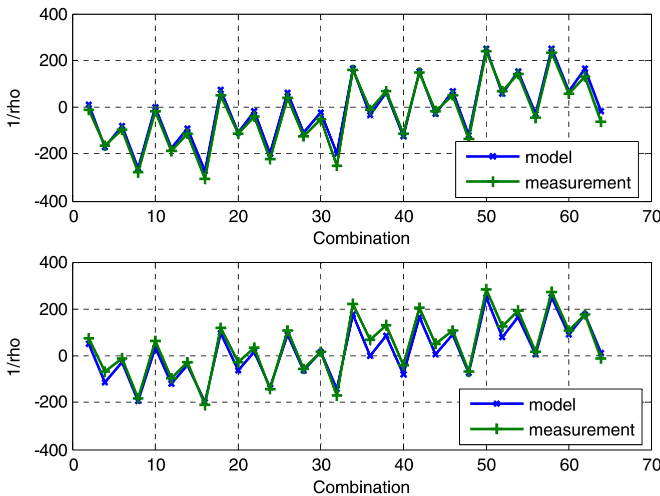

Figure 8. Beam curvature estimation with yield analysis ($K = 1.4$) at 20 °C (top) and 60 °C (bottom).

The residual stresses $\sigma(z)$ of metal layers are released when metal layers yield, so $\sigma(z)$ is modified to $\sigma'(z)$ when yield

$$(\sigma'(z) + \Delta\varepsilon E(z)) - \frac{E(z)}{\rho}(z - z_o) = Y \quad \text{for yield metal}$$
$$\Rightarrow \sigma'(z) = Y + \frac{S}{E}E(z) + \frac{E(z)}{\rho}(z - z_o). \tag{8}$$

$\sigma'(z)$ and ρ cannot be solved explicitly by (6) and (8) due to the yield condition. However, we may derive $\sigma'(z)$ and ρ at $T = T_2$ iteratively by (6) and (8) with an initial guess of ρ at $T = T_1$ near T_2. With the iteration, state transition for a given thermal history can be calculated. Figure 7 shows the simulated scenario of the CMOS MEMS packaging process with the thermal history $T_o \rightarrow 350$ °C $\rightarrow 20$ °C $\rightarrow 60$ °C. The last cycle (20–60 °C) simulates the measurement activity (20–60 °C) in the lab. The simulation considers both tensile and compressive yield of metal layers.

It is found that the residual stress of each metal layer after the thermal process varies. This indicates that the assumption of single residual stress of metal layers used in previous sections is not valid. With the yield analysis, we derive the beam curvature for each layer combination without extracting the residual stress from measurement, as shown in figure 8.

The estimation error of the model depends on the scaling factor K. With yield analysis in this section, similar

model accuracy without residual stress extraction is achieved with typical CTE scaled by $K = 1.4$. The scaling factor K compensates inaccuracy of CTEs and the temperature-dependent yield curve. The yield analysis model does not require any pre-condition or extraction of residual stresses since the residual stresses can be predicted by simulating the yield/annealing process. Estimation results in table 3 simplified the analysis with the same yield stress curve for each layer. However, temperature-dependent yield stress of the aluminum thin film is process dependent and varies for different layer thicknesses [13]. Extracting residual stresses for individual layers, as shown in section 3.4, is a more feasible approach for beam curvature estimation when detailed material yield data are not available.

4. CAS tool for analytical curvature modeling

Table 4 shows 10 Maxima CAS tool output examples of $2^6 = 64$ beam curvature formulas (R00001–R010011, the second to 20th combinations with M6 present) for the simplified model described in section 3.2, where all oxide layers and all metal layers have the same thicknesses t_o and t_m. Calculated formulas and extracted key parameters shown in section 3 can be used in the circuit simulator that provides CMOS MEMS designers accurate modeling of beam curvature based on the model extracted from the measurement results of silicon proven test structures.

5. Conclusion

In this paper, we have demonstrated the analytical model of temperature-dependent yield effects on the curvatures of composite beam structures used in CMOS MEMS. Yield analysis during the thermal process of CMOS MEMS packaging process is also modeled. Key parameters including the residual stresses and the scaling factor of the CTE that characterize the temperature-dependent effect of the beam curvature of the process can be extracted by measuring curvatures of a limited number of metal/oxide layer combinations. The models are verified with measurement results of the ASIC-compatible 0.18 μm 1P6M CMOS MEMS process before and after the high temperature packaging process. Beam curvature prediction in these models can be imported in EDA tools to model the temperature-dependent device characteristics such as sensing capacitance and spring constant of MEMS sensors for the monolithic sensor SOC design.

References

[1] Sun C-M, Tsai M-H, Liu Y-C and Fang W 2010 Implementation of a monolithic single proof-mass tri-axis accelerometer using CMOS-MEMS technique *IEEE Trans. Electron Devices* **57** 1670–9

[2] Huang C J, Wen K A, Cheng Y T, Chen J Y, Chang C S and Chou W C 2011 Standard 0.18 μm 1P6M CMOS IC foundry flow for accelerometer, analog readout circuit and wafer level capping package integration *Proc. IEEE on Sensors* pp 750–3

[3] Xie H, Erdmann L, Zhu X, Gabriel K J and Fedder G K 2002 Post-CMOS processing for high-aspect-ratio integrated silicon microstructures *J. Microelectromech. Syst.* 93–101

[4] Brand O 2006 Microsensor integration into systems-on-chip *Proc. IEEE* **94** 1160–76

[5] Fedder G K, Howe R T, King Liu T-J and Quévy E P 2008 Technologies for co-fabricating MEMS and electronics *Proc. IEEE* **96** 306–22

[6] Boser B E and Howe R T 1996 Surface micromachined accelerometers *IEEE J. Solid State Circuits* **31** 366–75

[7] Rebeiz G M and Muldavin J B 2001 RF MEMS switches and switch circuits *IEEE Microw. Mag.* **2** 59–71

[8] Feng Z-C and Liu H-D 1983 Generalized formula for curvature radius and layer stresses caused by thermal strain in semiconductor multilayer structures *J. Appl. Phys.* **54** 83–85

[9] DeVoe D and Pisano A 1997 Modeling and optimal design of piezoelectric cantilever microactuators *J. Microelectromech. Syst.* **6** 266–70

[10] Lakdawala H and Fedderc G K 1999 Analysis of temperature-dependent residual stress gradients in CMOS micromachined structures *Proc. 10th Int. Conf. on Solid State Sensors and Actuators Transducers (Jun 1999)* pp 101–11

[11] Scott S, Kim J-I, Sadeghi F and Peroulis D 2012 An analytical capacitance model of temperature-sensitive, large-displacement multimorph cantilevers: numerical and experimental validation *J. Microelectromech. Syst.* **21** 161–70

[12] MMPDS 2003 Metallic materials properties development and standardization *DOT/FAA/AR-MMPDS-01* US Department of Transportation

[13] Chu E C 1996 Temperature-depdendent yield properties of passivated aluminum thin films on silicon wafers *MS Thesis* Department of Materials Science and Engineering, Massachusetts Institute of Technology

[14] Chu W H and Mehregany M 1993 A study of residual stress distribution through the thickness of p +silicon films *IEEE Trans. Electron Devices* **40** 1245–50

[15] Fang W and Wickert J A 1996 Determining mean and gradient residual stresses in thin films using micromachined cantilevers *J. Micromech. Microeng.* **6** 301–9

[16] Huang S and Zhang X 2007 Gradient residual stress induced elastic deformation of multilayer MEMS structures *Sensors Actuators* **134** 177–85

[17] Fachin F, Nikles S A, Dugundji J and Wardle B L 2011 Analytical extraction of residual stresses and gradients in MEMS structures with application to CMOS-layered materials *J. Micromech. Microeng.* **21** 095017

[18] Huang S and Zhang X 2006 Extension of the Stoney formula for film–substrate systems with gradient stress for MEMS applications *J. Micromech. Microeng.* **16** 382

[19] Hsueh C-H 2002 Modeling of elastic deformation of multilayers due to residual stresses and external bending *J. Appl. Phys.* **91** 9652–6